Separately reconstructing the structural and functional parameters of a fluorescent inclusion embedded in a turbid medium

Baohong Yuan and **Quing Zhu**

Department of Electrical and Computer Engineering, University of Connecticut, Storrs, CT, 06269, USA, zhu@engr.uconn.edu

Abstract

We report a novel imaging technique for fluorescence diffuse optical tomography (FDOT). Unlike conventional FDOT, this technique separates the imaging procedure into two steps to respectively reconstruct the structural information (such as the center position and the radius), and the functional information (such as the fluorophore concentration and/or lifetime) of a fluorescing target embedded in a turbid medium. The structural parameters of the target were estimated from the amplitude ratio and phase difference of fluorescence signals received at different detectors, because the amplitude ratio and phase difference were found independent of, or weakly related to, the functional parameters. Based on the estimated structural parameters, a dual-zone mesh technique was utilized to reconstruct the fluorophore concentration. Results of simulations and phantom experiments showed that the structural parameters could be accurately recovered, without knowing the functional information, and that the reconstruction accuracy of the functional parameter was greater than 80%.

1. Introduction

Diffuse optical tomography (DOT) employs near infrared (NIR) diffused light to probe for functional information of biological tissues [1–7]. To further increase the target to background contrast, fluorescent diffusive optical tomography (FDOT) has been under intensive investigation [8–29]. Assisted by proper molecular probes, FDOT has been expanded to perform molecular imaging in small animals [17], and a new concept of fluorescent molecular tomography (FMT) has been introduced [18,19].

Ntziachristos *et al* have demonstrated [17–20] a method of imaging tumors in mice, targeted by special fluorescing probes, using the CW system. A sub-millimeter resolution and a high reconstruction accuracy of the fluorophore concentration were obtained when a charge-couple device (CCD) camera, with a large number of pixels or measurements (up to 10^6), was employed [20]. However, the imaging volume of 74 cm^3 was only adequate for imaging small animals [15]. In contrast, other research groups [11–13] have used the frequency domain technique and increased the imaging volume to 260 cm^3 and 1000 cm^3, which are clinically relevant [15]. Unfortunately, the reconstruction accuracy of the fluorophore concentration is much lower than that obtained by the CW method. For example, only ~20% of the expected value was recovered by Lee et al [11]. Approximate 46% and 140% of the expected values were obtained by Godavarty et al [13] for the imperfect uptake of fluorophore into the target (100:1) and for the perfect uptake (1:0), respectively. This low reconstruction accuracy may be caused by fewer measurements acquired over a larger imaging region; these were 7×30 (sources $\times$ detectors) measurements by Lee et al, and 27×128 by Godavarty et al. A commercially available time-domain fluorescence system specifically designed for small animal imaging, Explore Optix™, has been developed by the Advanced Research Technology

Inc [3]. From the temporal point spread function of the incident laser pulse, the structural and functional information of the inclusion can be obtained by this system. In addition, because a scanning system is adopted, the imaging region is adjustable. However, imaging a large region results in a lengthened data acquisition time. In addition, the cost of this system is significantly higher than the DC and FDPM systems.

To improve reconstruction accuracy of a fluorescence inclusion imbedded in a large imaging volume, we introduce, to the best of our knowledge, a novel technique to reconstruct the structural and functional parameters of a fluorescent target. Unlike conventional FDOT mentioned above, our new imaging technique separately reconstructs the structural parameters (such as center position and radius) and the functionally parameters (such as fluorophore concentration). The amplitude ratio and phase difference between the fluorescence signals received by different detectors are found to be independent of, or weakly depend upon, the fluorophore concentration. Therefore, the amplitude ratio and the phase difference are utilized to estimate the target's structural information without knowing the fluorophore concentration. With the target structural information available, a dual-zone mesh technique, previously developed by our group for optical absorption and scattering imaging [30–32], is employed to reconstruct the fluorophore concentration. By separating the imaging procedure into two steps, both the structural and functional parameters can be accurately recovered from 9 sources and 10 detectors. In addition, the total imaging volume can be expanded or localized, depending on the target volume and the design of the imaging probe.

This paper is organized as follows: the principle of estimating the structural parameters is introduced in 2.1, and the forward model and the inverse algorithm for reconstructing the functional parameters are presented in section 2.2. The simulation and experimental methods are detailed in section 3. The results and discussion are given in section 4, and a summary is provided in section 5.

2. Theories

2.1 Principles of estimating structural parameters of the inclusion

The new and important finding reported herein is that the ratio of fluorescence signals excited by a single source and received by two detectors depends only on the structural parameters of the inclusion, therefore, it can be used to estimate these parameters. The principle behind this finding is explained by the following theoretical analysis only when the fluorescence signals generated by the background fluorophore can be eliminated from the total fluorescence measurements (or there is perfect uptake of fluorophore into the target). When the elimination of the background signals is not feasible (or there is imperfect uptake of fluorophore into the target), the analyses based on calculations are also discussed in this section.

Assuming a spherical fluorescent target is embedded in a semi-infinite turbid medium, we define its structural parameters as center position (X, Y, Z) and radius α. The functional parameters of the target are fluorophore concentration in the target. According to diffusion theory [10,33], the fluorescence fluence excited by a point source located at r_S and detected by a detector located at r_D can be expressed by the following equation:

$$\varphi^{fl}(r_s, r_D) = \frac{S_0}{4\pi D_{ex} D_{fl}} \frac{\Lambda \varepsilon}{(1 - i\omega\tau)} \int_\Omega G_{ex}(r_s, r) G_{fl}(r, r_D) N(r) dr^3,$$

(1)

where r is a spatial variable and Ω represents the target region where fluorophore is located. S_0 is the source strength and D is the diffusion coefficient. Subscripts, "*ex*" and "*fl*", indicate

that the variables are measured at the excitation and emission wavelengths, respectively. Λ, τ, and ε are the quantum yield, the lifetime, and the extinction coefficient of the fluorophore, respectively. G is Green's function and $N(r)$ is the fluorophore concentration.

As an example, Fig. 1(a) shows a configuration of detecting fluorescence fluences excited by a source S1 modulated at a frequency ω and detected by two detectors D1 and D2. The ratio of the fluorescence fluences detected at D2 and D1 can be obtained as:

$$\frac{\varphi^{fl}(r_{S1},r_{D2})}{\varphi^{fl}(r_{S1},r_{D1})}=\frac{\int_{\Omega}G_{ex}(r_{S1},r)G_{fl}(r,r_{D2})N(r)dr^3}{\int_{\Omega}G_{ex}(r_{S1},r)G_{fl}(r,r_{D1})N(r)dr^3}.$$

(2)

From Eq.(2) we can see that the only difference between the numerator and the denominator is the term G_{fl} that includes the positions of the two different detectors. Therefore, we can expect that the ratio of the fluorescence fluences is mainly dependent on G_{fl}, rather than G_{ex} and $N(r)$. The results presented in section 4 will further validate this observation. For convenience we define two variables to describe the ratio of the fluorescence fluences: the amplitude of the ratio, R, and the phase of the ratio, $\Delta\Psi$. They can be written as:

$$R=|\frac{\varphi^{fl}(r_{S1},r_{D2})}{\varphi^{fl}(r_{S1},r_{D1})}|$$

(3)

$$\Delta\Psi=phase\left[\frac{\varphi^{fl}(r_{S1},r_{D2})}{\varphi^{fl}(r_{S1},r_{D1})}\right].$$

(4)

Based on an analytical solution of the coupled diffusion equations (see Appendix and Ref. [33]) and the configuration given in Fig. 1(a), we have calculated R and $\Delta\Psi$ as functions of the target depth (Z) and radius (α), shown in Fig. 1(b). In the calculations, a semi-infinite geometry and an extrapolated boundary condition were adopted [34,35]. The background parameters of the medium used in the calculations can be found in Table 1. These values correspond to the measured values of 0.5% Intralipid solution. As expected, the R and $\Delta\Psi$ depend on the depth and radius of the inclusion (X and Y are fixed at the origin in this example). Since the fluorophore concentration in the target was needed to compute the wave vectors of $k_{in\_ex,fl}$ in Eq.(A3), we varied the target concentration from 0.01 to 10 μM and did not find significant changes in Fig. 1(b), except when the target was very close to the surface. This result suggests that R and $\Delta\Psi$ are independent of the fluorophore concentration inside the target, and it will be further discussed in section 4.1.1. In addition, we also calculated R and $\Delta\Psi$ with different background parameters (see Fig. 1(c)), and similar results were obtained. Fig. 1(d) shows the calculated R and $\Delta\Psi$ as a function of target radius. It can be seen that both R and $\Delta\Psi$ are weakly related to target radius.

When the elimination of the background signals is not feasible, the analyses of R and $\Delta\Psi$ are not straightforward, as when background signals can be subtracted from total measurements. However, from calculations we find that the effects of the background fluorophore concentration on R are considerably small when the background concentration is much lower than that in the target. The calculations are based on the analytical solution given in the Appendix and the configuration shown in Fig. 1(a). The results, as an example, are presented in Fig. 1(e). The coordinates of the two detectors and the source are presented in the figure and

other background parameters used in the calculation can be found in Table 1. The squares (solid and open) are results of the perfect uptake of fluorophore into the target, and the ratio of concentration in the target to that in the background is 1:0. Similarly, the circles and up-triangles are results from an imperfect uptake, and the target to background concentration ratios used are 1:0.005 and 1:0.01, respectively, which are typical values reported in the literature [11, 13,14]. It is clear that the effects of the background concentration on the amplitude ratios are negligible when the detectors are further away from the source (open symbols). When the detector pair is closer to the central source (solid symbols), the amplitude ratios are affected by the background concentration only when the target depths are larger than 1.4 cm. This result indicates that when the background signal cannot be eliminated, we should use the source-detector pairs with longer separation distances to estimate the structural parameters. On the other hand, the effect of background concentration on $\Delta\Psi$ is more pronounced than on R when the concentration ratio is 1:0.01. Therefore, the use of $\Delta\Psi$ should be avoided when the background concentration is high. When multiple sources and detectors are employed in experiments, we can select different combination of any two detectors and any source to obtain the ratios of fluorescence fluences. Therefore, in principle, multiple ratios of fluorescence fluencs can be used to recover the structural parameters. The chi-square (χ^2) fitting technique was used to estimate the target structural parameters from multiple measurements. In the χ^2 fitting procedure, the errors between the measured data (R s and $\Delta\Psi$ s) and the generated data from the analytical solution of the coupled diffusion equations were minimized (see Appendix and Ref. [33]) by varying the unknown structural parameters [36,37]. A simple optimization algorithm, Simplex Down-Hill [36,37], was used for minimization. When the background signals cannot be subtracted from the total measurements, both concentrations inside and outside the target (N_{in} and N_{bg}) are needed in the calculation of the theoretical data R and $\Delta\Psi$. We set the concentrations as two unknown constants and estimate them in the fitting procedure. Thus six unknowns (X, Y, Z, α, N_{bg}, and N_{in}) are estimated simultaneously in the fitting procedure. We find that the estimated structural parameters are quite acceptable, as will be shown in section 4. However, the estimated concentrations are generally unacceptable. This result further implies that the structural parameters are strongly related to R and $\Delta\Psi$, and the fluorophore concentrations are weakly related to R and $\Delta\Psi$.

2.2 The forward model and the inverse algorithm for functional imaging

To demonstrate the principle of our new reconstruction scheme, we focus on the reconstruction of fluorophore concentration and lifetime is considered as a constant. To reconstruct the fluorophore concentration, a normalized Born approximation has been widely used in the literature [10,11,14]. Specifically, the equation (1) was discretized and normalized by a set of measurements for elimination of unknown system parameters, such as source strengths and detector gains. Several normalization schemes have been proposed [11,14], and we adopted the simplest scheme for phantom experiments in which the measurement was made from a homogeneous fluorescent solution and was used to normalize the heterogeneous measurement. For clinical or animal studies, other advanced normalization [11,14] schemes can be applied. Equation (5) is the normalized Born approximation technique used in this paper:

$$\frac{\varphi^{fl}}{\varphi_0^{fl}} = \sum_j \left(\frac{\left(k_{ex}^2 - k_{fl}^2\right)\Delta v}{4\pi N_0^{fl}} \cdot \frac{G_j(r_s,r_j)G_j(r_j,r_d)}{\left[\left(G_{ex}(r_s,r_d) - G_{fl}(r_s,r_d)\right)\right]} \right) \cdot N(r_j),$$

(5)

where $k_{ex(fl)} = \sqrt{\left(-\mu_{\alpha\_ex(fl)} + i\omega/v\right)/D_{ex(fl)}}$ is the wave vector of the diffuse photon density wave at the wavelength of the excitation (emission). $\mu_{\alpha\_ex(fl)}$ is the absorption coefficient of the background medium at the wavelength of the excitation (emission). ω and v are the modulation

frequency of the source and the speed of the light in the medium, respectively. Δv is the volume of each voxel, and N_0^{fl} is the calibrated fluorophore concentration in the homogeneous medium and is used for normalization of the heterogeneous data.

A dual-zone mesh method was reported to significantly improve the reconstruction accuracy [29–32] when the *a priori* target structure location is given. We have used the dual-zone mesh method in this study because the target structure is readily available from the estimation technique described in section 2.1. In the dual-zone mesh scheme, we divide the imaging region into two parts, L and B, where L is the target region and B is the background region. We then discretize the target region into a finer grid ($0.1\times0.1\times0.5$cm) and the background region into a coarser grid ($1.0\times1.0\times0.5$cm). Therefore, Eq.(5) can be further expressed as a linear matrix equation when multiple measurements are available:

$$[M]_{T\times1} = [W_L, W_B]_{T\times N_0} [X_L, X_B]_{N_0\times1},$$

(6)

where M corresponds to the value on the left side of Eq. (5). W_L and W_B are weight matrices for the target region and the background region, respectively, and have dimensions of $T\times N_L$ and $T\times N_B$, respectively. T is the total measurement. N_L and N_B are the total numbers of voxels in the target region and the background region, respectively. $N_0=N_L+N_B$ is the total number of voxels. $[X_L]$ and $[X_B]$ are vector representation of the distribution of fluorophore concentration in the target region and the background region, respectively. By using a dual-zone mesh, we can maintain the total number of voxels with unknown concentration on the same scale of the total measurements. As a result, the inverse problem is less underdetermined. In general, only a few iterations are needed for reconstruction to converge to a stable solution. The total least-square method and the conjugate gradient technique are used to iteratively solve Eq.(6) [30–32]. Note that this dual-zone mesh technique [29–32] should not be confused with a multi-grid technique [11,40]. The multi-grid technique was used in the literature to improve calculation efficiency of the forward weight matrix, especially when a finite difference or finite element technique was used [11,40].

3. Methodology

We have designed a probe with 9 sources and 10 detectors (see Fig. 2). The total imaging volume is 324 cm^3 ($9\times9\times4$ cm^3). In fact, the imaging volume can be increased or decreased by adjusting the distribution of sources and detectors on the probe, as long as the signal to noise ratio is acceptable for those detectors with larger source-detector separations. For each source, a total of 45 (C_{10}^2) amplitude ratios and 45 phase differences can be obtained. Thus, a total of 810 ($9\times45\times2$) measurements can be completed to determine the structural parameters (X, Y, Z, a), which is an over-determined problem. Because both amplitudes and phases are used in the imaging of the fluorophore concentration, the maximum number of measurements is 180 ($9\times10\times2$).

3.1 Simulation Method

To evaluate the performance of our technique, we generated the fluorescence fluences from the analytic solution given in the Appendix and Ref. [33]. Five percent independent random Gaussian noise was added to both the real and imaginary parts of the data. The amplitude ratio R and phase difference $\Delta\Psi$ were calculated from the simulated data and used to estimate the structural parameters. This procedure was repeated five times and the mean and the standard deviation of each estimated parameter were obtained. All the background parameters of the medium used in the calculations were listed in Table 1. These parameters correspond to the

fluorescent dye Cy5.5, which will be described later. The fluorophore concentrations of the target were set as 5 μM inside, and 0.023 μM outside.

3.2 Experimental Method

Based on our previous frequency-domain system designs [32,38], we constructed a simple frequency-domain system. A pigtailed laser diode of 660 nm (Thorlabs Inc) was used as the excitation, which was modulated at 140.00 MHz, and an optical switch (Piezosystem Jena) was used to sequentially deliver the light to 9 source positions. A photon-multiplier tube (PMT, Hamamatsu R928) was chosen as the detector. Two aspherical lenses (Edmund, NT43-987) were utilized to collimate the fluorescence photons collected by the detector-fiber. Two interference optical band-pass filters (Omega Optical Inc, 695 BP10, CVI Laser Inc, F03-694.3-4) were mounted together serially and placed between the two aspherical lenses to block the excitation photons and pass emission photons. The total optical density (OD) was larger than 8. The system was controlled by LABVIEW (National Instrument Inc). For each source-detector pair, the raw data acquisition was repeated 5 times. Thus, the means of the amplitude and phase were obtained and used to calculate the amplitude ratio R and the phase difference $\Delta\Psi$.

In the phantom study, 0.5% Intralipid solution was used to simulate a semi-infinite medium. A hollow and transparent cube $0.8 \times 0.8 \times 0.8$ cm^3 was filled with Intralipid at the same concentration. A fluorescent dye of Cy5.5 (Amersham Biosciences, PA15601) was dissolved in the cube, which was submerged into the Intralipid solution. A three dimensionally adjustable micrometer was used to control the X, Y, and Z positions. The calculated concentration of Cy5.5 in the cube was 5 μM. The background concentration was controlled at 0.023 μM.

We performed three sets of measurements for estimating target structural parameters and imaging fluorescence concentration. The first set of measurements was made from the 0.5% Intralipid solution without Cy5.5 and the cube, and the measured signals should be considered as the leakage of excitation light from the two optical filters. The second set of measurements was made from the same 0.5% Intralipid solution with 0.023 μM Cy5.5 dissolved in the solution, but without submerging the cube. This set of measurements consisted of the leakage signals and the fluorescence signals generated by the background fluorophore. Subtracting the first set of signals from the second set, we obtained the background fluorescence signals that were used to normalize the measurements when the fluorescence target was submerged. The third set of measurements was made with the same conditions as the second set, but with the cube submerged in the Intralipid solution. This set of measurements consisted of leakage signals, the fluorescence signals generated from the background fluorophore, and fluorescence signals generated by the fluorophore in the cube. The leakage of the excitation light was always considered as noise and eliminated from the measurement. After subtracting the leakage signals from the third measurements, the remaining signals were used to retrieve the amplitude and phase of fluorescence signal for imaging the fluorophore concentration, and were used to calculate Rs and $\Delta\Psi$s for estimating the structural parameters. The homogeneous (background) measurement is used for normalization or calibration. In this paper, we refer both the simulated data with noise added and the phantom experimental data as measured data to distinguish them from the data without adding noise and calculated by the analytical solution (A1)–(A4).

4. Results and Discussions

4.1 Simulation results

4.1.1 Estimation of the structural parameters—Figure 3 shows the estimated structural parameters versus their true values. In Fig. 3(a), we varied the target's X and Y positions from

−0.8 to 1.0 cm, while maintaining the depth and radius as 1.0 and 0.4 cm, respectively. The line with solid circles (blue) represents the target's true X and Y positions, and the open circles (red) are the values of X and Y estimated by the data with noise. The corresponding values of the estimated depth Z and radius α are also given in the figure. For each target's position, the estimated values are scattered around the true values. When the error is defined as the difference between the mean of the estimated values and the true position, the maximum error in X is 0.047 cm, and in Y is 0.065 cm. This implies that the estimation of the X and Y positions are highly accurate. Similarly, in Fig. 3(b), we varied the target depth Z and maintained X = Y =0 cm and α = 0.4 cm. The line with solid circles (blue) denotes the ideal results, and the open circles (red) represent the estimated results. The estimated values of X, Y and α and the corresponding standard deviations are also shown in the figure. Two dotted lines are used to indicate the diameter of the spherical target. It is evident that the estimated depths in Fig. 3(b) agree well with the true values. All the estimated values are within the region occupied by the target. Only when the target has a depth of 0.5 cm does the estimated value have a larger standard deviation.

This result may be attributed to the fact that the effect of the fluorophore concentration of the target on the amplitude ratio and phase difference is significant for those measurements with separation distances between the target and the detectors comparable to the radius of the target when the target is very close to the boundary. The estimated radii are given in Fig. 3(c), where X, Y and Z are fixed, and α is varied from 0.2 to 1.0 cm. The line with solid circles (blue) represents the ideal results and the open circles (red) show the estimated results. In general, the estimated mean radii have large errors and large standard deviations, which suggests that the estimation accuracy of the radius is lower than those of X, Y, and Z. It implies that the correlation of the amplitude ratio and phase difference with the target radius is relatively weaker compared with X, Y and Z. This result can be explained from Eq.(2), where the integral region Ω or target region, which is related to the target radius, occurs in both the numerator and the denominator. Fortunately, the reconstruction of the fluorophore concentration in the following step only requires an approximate target size, because the imaging region is chosen much larger than the true size.

4.1.2 Reconstruction of the fluorophore concentration—A spherical target with a radius of 0.4 cm and a concentration of 5 μM was imaged and the background concentration of fluorophore was 0.023 μM. The parameters of the Cy5.5 listed in Table 1 were used in the reconstruction. The target was located at the center of the imaging region (X=Y=0.0 cm) and the target depth was 2.5 cm. The reconstructed images in X-Y plane at different depths are shown in Figure 4 (a). The reconstructed target appears only on the fifth slice, which corresponds to the imaging depth of 2.5 cm and is identical to the true target depth. Since the radius of the target is 0.4 cm, we should not expect any target mass in the fourth and the sixth layers because other slices are background regions. The percentage of the maximum reconstructed concentration with respect to its true value (5 μM) is 88.54%. The average of the reconstructed values within the full width at half maximum (FWHM) is 67.39%. For a comparison, the reconstructed images obtained from the conventional reconstruction technique (single mesh, 0.25×0.25×0.5 cm^3) were shown in Fig. 4.(b). The reconstructed images spread into three layers and the percentage of the maximum reconstructed value of each layer is 9.58%, 36.97%, and 12.14%, respectively, which is close to the results reported in Refs. [11,13] but is much lower than dual-zone mesh results shown in Fig. 4 (a). In order to examine the effect of the background parameters on the images, we show a set of images in Fig. 4 (c) that are

reconstructed based on the following parameters: μ'_{s_ex}=10, μ_{α_ex} = 0.02, μ'_{s_fl}=9, and μ_{α_fl} = 0.035 cm^{-1}. The percentage of the maximum reconstructed concentration is 90.25%. The average of the reconstructed values within FWHM is 73.06%. In addition, we have varied the target depth and repeated the imaging processes and obtained similar results.

4.1.3 Estimation and reconstruction of two targets—In order to examine the feasibility of our new technique for reconstructing multiple targets, we positioned one spherical target at −0.4 (X), 0.0 (Y) and 1.5 (Z) cm, and the other at X=0.4 (X), 0.0 (Y) and 1.5 (Z) cm. The radius of each target is 0.4 cm. They were represented by two red dashed circles shown in Fig. 5(a). The fluorophore concentration was 5.0 μM in the left target and 4.0 μM in the right one. The forward data was generated by numerically calculating the integral in Eq.(1) with five percent random Gaussian noise added. The same methods as discussed in Sec.2 were used to estimate the structural and fluorophore concentration distribution. The black dashed square indicated the region where the sources and the detectors were distributed. The green dashed square represented the target region L where the fine-mesh image was reconstructed. The estimation of the structural parameters was repeated five times and five estimated X-Y positions were shown by blue dots in Fig. 5(a). The estimated averages and standard derivations of the depth and radius were presented in Fig. 5(a). Since we used one target to approximate the two targets, we do expect to obtain the center positions of the two targets, but an approximate equivalent center position for two targets. All the estimated X-Y positions in Fig. 5(a) were between the centers of the two targets. This is good enough for us to localize the two targets by an appropriate target region L marked by the green dashed square. Within this region, the fluorophore concentration distribution was reconstructed and shown in Fig. 5 (b). The maximum reconstructed concentrations for the two targets are 95.57% and 87.48%, respectively.

4.2 Experimental results

4.2.1 Recovery of the structural parameters—We simultaneously changed the target positions X and Y, and controlled the target at a depth of approximately 1.98 cm (measured from the micrometer). Figure 6 (a) provides the estimated X and Y values versus their expected values. The blue circles indicate the measured center positions of the cube in the X-Y plane and the error bars along X and Y denote the length and width of the cube. The red squares show the estimated positions of the cube; the estimated depth and radius are also shown and the numbers in parentheses are the corresponding standard deviations. It can be seen that the estimated X and Y are considerably close to their expected values. The estimated depth Z and radius α are also close to the expected values of 1.98 cm and 0.4 cm, respectively. In view of the fact that light propagation in the highly scattering medium is governed by diffusion theory, we do not attempt here to obtain an exact shape of the cube. Therefore, the expected "radius" of the cube is considered as half the thickness of the cube. In Fig. 6(b), we controlled X=0.24 cm and Y=−0.33 cm, and varied the depth Z. The dashed line with solid circles represents the ideal results and the red squares show the estimated depths. Two dotted lines are used to indicate the thickness of the target. The target occupies the region within the two dotted lines. It can be seen that all estimated values are within the occupied regions of the cube. Relatively large errors are evident when the target is located at a greater depth; this is reasonable, because a deep target generates weaker signals than a shallow one. Note that in order to avoid the effect of the background concentration on the amplitude ratio and phase difference, only those measurements with the distances longer than 1.5 cm were used. In addition, to preserve high signal to noise ratio of the data, only those measurements with distances shorter than 3.0 cm were use in the estimation of the structural parameters.

4.2.2 Reconstruction of the fluorophore concentration—An example of the reconstructed images from the experimental data is shown in figure 7. The center of the target is located at X= 0.24 cm, Y= −0.33 cm, and Z=2.65 cm and the target is a 0.4×0.4×0.4 cm^3 cube. The imaging depth of each slice is the same as used in Fig. 4. From Fig. 7 (a) (dual-zone mesh), we can see that the reconstructed images appear in both fifth and sixth slices, which correspond to the imaging depth of 2.5 cm and 3.0 cm. This result agrees with the target location which has occupied two layers. Other slices are the background regions. The percentage of the

maximum reconstructed concentration with respect to its true value ($5\ \mu M$) is 93.37% and 94.85% in the fifth and the sixth slices, respectively. The corresponding average of the reconstructed concentrations within the FWHM is 68.57% and 70.21%, respectively. The reconstruction results using a single mesh from the same data are shown in Fig. 7(b). The reconstructed images occupied the third, fourth and fifth layers and the percentage of the maximum reconstructed value relative the true value is 15.53%, 48.45% and 18.92%, respectively. These values are close to the results reported in Refs. [11,13] but are much lower than the values obtained from the dual-zone mesh shown in Fig. 7 (a). In addition, we have moved the target to different depths of 1.6 cm and 1.98 cm, respectively, and repeated the imaging processes. Similar results were obtained.

5. Summary

In summary, we presented, to the best of our knowledge, a novel technique that separates the imaging procedure into two steps. In the first step, the amplitude ratio and phase difference between the fluorescence signals received at two detectors, and excited by a single source, were used to extract the structural parameters of a target, because the amplitude ratio and phase difference were independent of, or weakly related to, the fluorophore concentration. Based upon the extracted structural parameters, the imaging volume was divided into two regions: target and background. With this dual-zone mesh technique, the distribution of the fluorophore concentration was reconstructed by using the normalized Born approximation. Simulation and phantom results showed that this technique is able to provide highly accurate values of both target location and fluorophore concentration.

Since the analytical solution of a spherical target is used to estimate the structural parameters, this may give certain errors when the target has an irregular shape. Also, we have assumed the concentrations both inside and outside the target were constant in the estimation of the structural parameters. This may results in certain errors in the estimation of the center position of the target. These limitations can be overcome if we use multiple targets in our forward model, which will be discussed in a future publication.

To compare with other's work (9, 11, 13), we adopted three typical concentration contrasts (1:0, 200:1, and 100:1) that were often used in the literature (see Ref.[13] for a detailed review). In general, the reconstruction accuracy of the structural and functional parameters is affected by the contrast [36]. For cases of lower contrast, we suggest to use the source-detector pairs with larger separation to avoid the strong background fluorescence signal. With the single detector system used in acquiring the reported experimental data, we could not perform *in vivo* studies. Currently, we are upgrading the single channel system to multiple detection channels and will perform *in vivo* studies to further validate this technique.

Acknowledgments

References and links

1. Massoud TF, Gambhir SS. Molecular imaging in living subjects: seeing fundamental biological processes in a new light. Genes Dev 2003;17:545–580. [PubMed: 12629038]

2. Weissleder R, Mahmood U. Molecular Imaging. Radiology 2001;219:316–333. [PubMed: 11323453]

3. Long, W.; Vernon, M. Optical molecular imaging: time domain advantages with explore Optix™. Advanced Research Technology Inc. Jan. 2004 http://www.art.ca/en/products/INOPaper040129.pdf

4. Skoch J, Dunn A, Hyman BT, Bacskai BJ. Development of an optical approach for noninvasive imaging of Alzheimer's disease pathology. J Biomed Opt 2005;10:011007-1-7.

5. Yodh A, Chance B. Spectroscopy and Imaging with Diffusing light. Phys Today 1995;3:34–40.

6. Tromberg N, Shah R, Lanning A, Cerussi J, Espinoza T, Pham L, Svaasand, Butler J. Non-Invasive in vivo characterization of breast tumors using photon migration spectroscopy. Neoplasia 2000;2:26–40. [PubMed: 10933066]

7. Murphy, B. Fundamentals of light microscopy and electronic imaging. Wiley-Liss; 2001.

8. Houston JP, Thompson AB, Gurfinkel M, Sevick-Muraca EM. Sensitivity and depth penetration of continuous wave versus frequency-domain photon migration near-infrared fluorescence contrast-enhanced imaging. Photochem and Photobiol 2003;77:420–430.

9. Milstein AB, Seungseok Oh, Webb KJ, Bouman CA, Zhang Q, Boas DA, Millane RP. Fluorescence Optical Diffusion Tomography. Appl Opt 2003;42:3081–3094. [PubMed: 12790460]

10. O'Leary MA, Boas DA, Li XD, Chance B, Yodh AG. Fluorescence lifetime imaging in turbid media. Opt Lett 1996;21:158–160.

11. Lee J, Sevick-Muraca EM. Three-dimensional fluorescence enhanced optical tomography using referenced frequency domain photon migration measurements at emission and excitation wavelengths. J Opt Soc Am A 2002;19:759–771.

12. Eppstein MJ, Hawrysz DJ, Godavarty A, Sevick-Muraca EM. Three-dimensional, Bayesian image reconstruction from sparse and noisy data sets: near-infrared fluorescence tomography. Proc Natl Acad Sci USA 2002;99:9619–9624. [PubMed: 12105269]

13. Godavarty A, Eppstein MJ, Zhang C, Theru S, Thompson AB, Gurfinkel M, Sevick-Muraca EM. Fluorescence-enhanced optical imaging in large tissue volumes using a gain-modulated ICCD camera. Phys Med Biol 2003;48:1701–1720. [PubMed: 12870578]

14. Ntziachristos V, Weissleder R. Experimental three-dimensional fluorescence reconstruction of diffuse media by use of a normalized Born approximation. Opt Lett 2001;26:893–895. [PubMed: 18040483]

15. Gurfinkel M, Ke S, Wen X, Li C, Sevick-Muraca EM. Near-infrared fluorescence optical imaging and tomography. Dis Markers 2003 2004;19:107–121. [PubMed: 15096708]

16. Sevick-Muraca M, Lopez G, Reynolds JS, Troy TL, Hutchinson CL. Fluorescence and absorption contrast mechanisms for biomedical optical imaging using frequency-domain techniques. Photochem and Photobiol 1997;66:55–64.

17. Graves E, Weissleder R, Ntziachristos V. Fluorescence molecular imaging of small animal tumor models. Curr Mol Med 2004;4:419–430. [PubMed: 15354872]

18. Ntziachristos V, Tung C, Bremer C, Weissleder R. Fluorescence molecular tomography resolves protease activity in vivo. Nat Med 2002;8:757–760. [PubMed: 12091907]

19. Mahmood U. Near infrared optical applications in molecular imaging, earlier, more accurate assessment of disease presence, disease course, and efficacy of disease treatment. IEEE Eng Med Biol Mag 2004;23:58–66. [PubMed: 15508386]

20. Graves E, Ripoll J, Weissleder R, Ntziachristos V. A submillimeter resolution fluorescence molecular imaging system for small animal imaging. Med Phys 2003;30:901–911. [PubMed: 12772999]

21. Ntziachristos V, Weissleder R. Charge-coupled-device based scanner for tomography of fluorescent near-infrared probes in turbid media. Med Phys 2002;29:803–809. [PubMed: 12033576]

22. Ntziachristos V, Schellenberger EA, Ripoll J, Yessayan D, Graves E, Bogdanov A, Josephson JL, Weissleder R. Visualization of antitumor treatment by means of fluorescence molecular tomography with an annexin V-Cy5.5 conjugate. Proc Natl Acad Sci USA 2004;101:12294–12299. [PubMed: 15304657]

23. Schulz RB, Ripoll J, Ntziachristos V. Experimental fluorescence tomography of tissues with noncontact measurements. IEEE Trans Med Imaging 2004;23:492–500. [PubMed: 15084074]

24. Schulz RB, Ripoll J, Ntziachristos V. Noncontact optical tomography of turbid media. Opt Lett 2003;28:1701–1703. [PubMed: 13677542]

25. Milstein B, Stott JJ, Oh S, Boas DA, Millane RP, Bouman CA, Webb KJ. Fluorescence optical diffusion tomography using multiple-frequency data. J Opt, Soc Am A 2004;21:1035–1049.

26. Hawrysz DJ, Eppstein MJ, Lee J, Sevick-Muraca EM. Error consideration in contrast-enhanced three-dimensional optical tomography. Opt Lett 2001;26:704–706. [PubMed: 18040426]

27. Lam S, Lesage F, Intes X. Tim domain fluorescent diffuse optical tomography: analytical expressions. Opt Express 2005;13:2263–2275.

28. Patwardhan SV, Bloch SR, Achilefu S, Culver JP. Time-dependent whole-body fluorescence tomography of probe bio-distributions in mice. Opt Express 2005;13:2564–2577.

29. Joshi, Bangerth W, Sevick-Muraca EM. Adaptive finite element based tomography for fluorescence optical imaging in tissue. Opt Express 2004;12:5402–5417.

30. Zhu Q, Huang M, Chen NG, Zarfos K, Jagjivan B, Kane M, Hegde P, Kurtzman SH. Ultrasound-guided optical tomographic imaging of malignant and benign breast lesions. Neoplasia 2003;5:379–388. [PubMed: 14670175]

31. Zhu Q, Chen NG, Kurtzman S. Imaging tumor angiogenesis using combined near infrared diffusive light and ultrasound. Opt Lett 2003;28:337–339. [PubMed: 12659436]

32. Chen NG, Guo P, Yan S, Piao D, Zhu Q. Simultaneous near infrared diffusive light and ultrasound imaging. Appl Opt 2001;40:6367–6280. [PubMed: 18364946]

33. Li XD, O'Leary MA, Boas DA, Chance B, Yodh AG. Fluorescent diffuse photon density waves in homogeneous and heterogeneous turbid media: analytic solutions and applications. Appl Opt 1996;35:3746–3758.

34. Haskell RC, Svaasand LO, Tsay T, Feng T, McAdams MS, Tromberg BJ. Bondary conditions for the diffusion equation in radiative transfer. J Opt Soc Am A 1994;10:2727–2741.

35. Passchens JCJ, 't Hooft GW. Influence of boundaries on the imaging of objects in turbid media. J Opt Soc Am A 1998;15:1797–1812.

36. Li X, Chance B, Yodh AG. Fluorescent Heterogeneities in Turbid Media: Limits for Detection, Characterization, and Comparison with Absorption. Appl Opt 1998;37:6833–6844. [PubMed: 18301500]

37. Press, WH.; Teukolsky, SA.; Vetterling, WT.; Flannery, BP. Numerical Recipes in C. Cambridge U. Press; New York: 1992.

38. Chen NG, Huang MM, Xia H, Piao D, Zhu Q. Portable near-infrared diffusive light imager for breast cancer detection. J Biomed Opt 2004;9:504–510. [PubMed: 15189088]

39. Yuan B, Zhu Q. Emission and absorption properties of indocyanine green in Intralipid solution. J Biomed Opt 2004;9:497–503. [PubMed: 15189087]

40. Paithankar DY, Chen AU, Pogue BW, Patterson MS, Sevick-Muraca EM. Imaging of fluorescent yield and lifetime from multiply scattered light reemitted from random media. Appl Opt 1997;36:2260–2272. [PubMed: 18253202]

Appendix

When a spherical fluorescing target with a radius α is embedded into a highly scattering medium with an infinite geometry, the fluorescence fluence detected at r_d and excited by a point source at r_s with a modulation frequency ω can expressed as [33]

$$\varphi^{fl}(r_s,r_d)=\varphi^{fl}_{out}(r_s,r_d)+\varphi^{fl}_{in}(r_s,r,r_d) \tag{A1}$$

$$\varphi^{fl}_{out}(r_s,r_d)=\frac{S_0}{D_{ex}D_{fl}}\frac{\Lambda\sigma N_{bg}}{(1-i\omega\tau)}\frac{1}{4\pi}\frac{1}{\left(k^2_{ex}-k^2_{fl}\right)}\times\left[\left(G_{ex}(r_s,r_d)-G_{fl}(r_s,r_d)\right)\right] \tag{A2}$$

$$\varphi_{inside}(r_s,r,r_d) = S_0 \frac{\Lambda\sigma N_{in}}{1-i\omega\tau} \frac{\alpha^2}{k_{in\_ex}^2 - k_{in\_fl}^2}$$
$$\times \sum_{lm}\left\{\left[k_{in\_fl}j_l(k_{in\_ex}\alpha)j_l'(k_{in\_fl}\alpha) - k_{in\_ex}j_l'(k_{in\_ex}\alpha)j_l(k_{in\_fl}\alpha)\right]\right.$$
$$\left.\times R_l^{ex}R_l^{fl}h_l^{(1)}(k_{out\_fl}|r_d-r|)h_l^{(1)}(k_{out\_ex}|r_s-r|)Y_{lm}(\Omega_{d,r})Y_{lm}^*(\Omega_{s,r})\right\}$$

(A3)

$$G_{ex(fl)}(r_s,r_d) = \frac{\exp(ik_{ex(fl)}|r_s-r_d|)}{|r_s-r_d|}$$

(A4)

Subscripts, "*in*" and "*out*", denote the inside and outside of the spherical inclusion, respectively. Subscripts, "*ex*" and "*fl*", indicate that the variables are measured at the excitation and emission wavelengths, respectively. k is the wave vector. N_{bg} and N_{in} are the concentrations of fluorophore in the background and the inclusion, respectively. R_l^{ex}, R_l^{fl}, j_l, j_l', $h_l^{(1)}$, $h_l'^{(1)}$, Y_{lm}, and Y_{lm}^* are special functions (see a detailed description about equations (A1–A4) in Ref. [33]). Other parameters are same as in equation 1. Based on equations (A1–A4) and an extrapolated boundary condition with a semi-infinite geometry [34, 35], the amplitude and phase of the fluorescence photon density wave at any position can be obtained and therefore the amplitude ratio R and phase difference $\Delta\Psi$ at any two positions can be calculated.
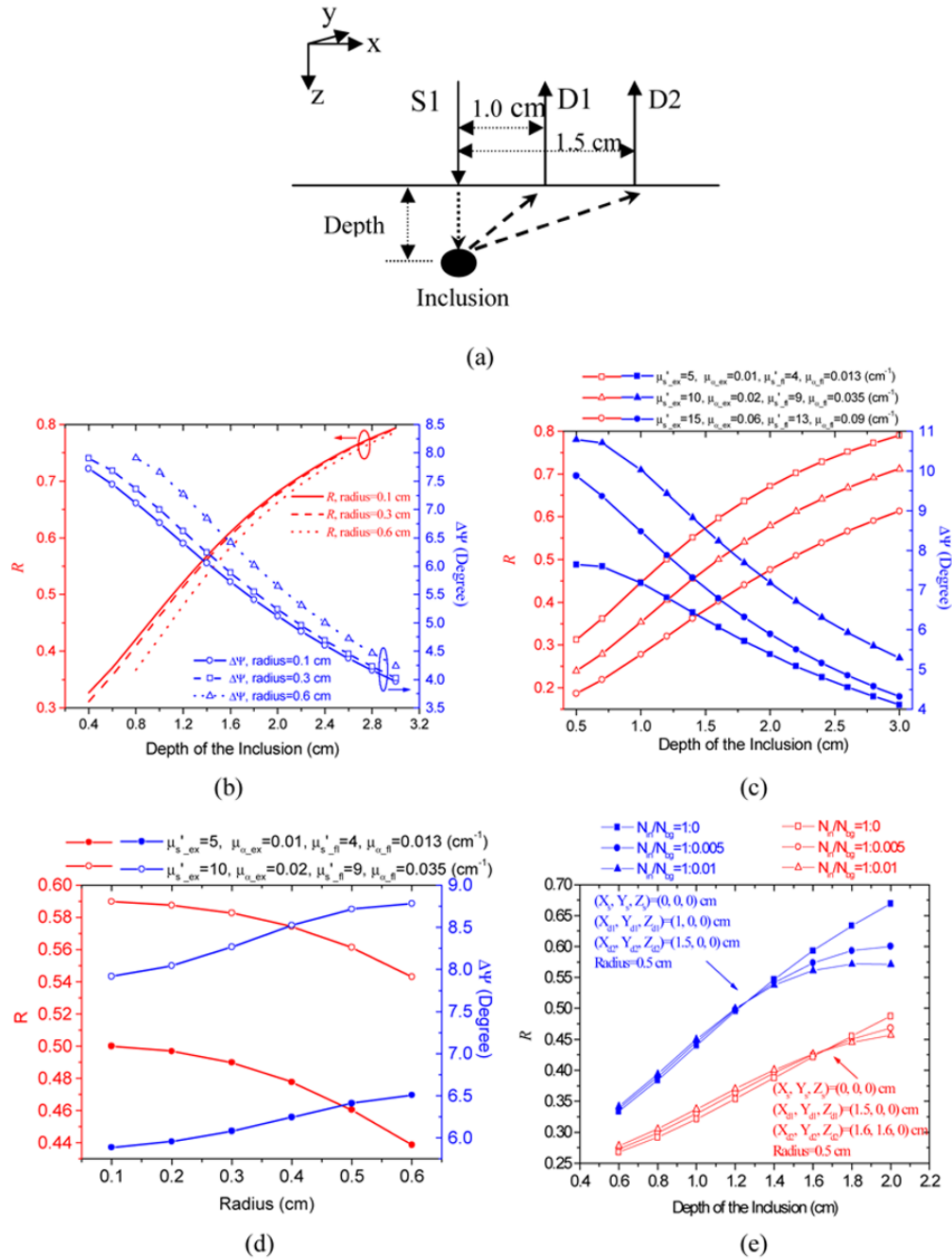
Fig. 1.
(a) Configuration of a source and two detectors for calculating R and $\Delta\Psi$ in (b)–(e). (b) Calculated results of R and $\Delta\Psi$ as a function of the target depth and the radius. The background concentration of fluorophore is zero. (c) Calculated R and $\Delta\Psi$ as a function of the target depth with different background parameters (the target radius is 0.4 cm). (d) Calculated R and $\Delta\Psi$ as a function of the target radius with different background parameters (the target depth is 1.5 cm). (e) Calculated R as a function of the inclusion depth at different ratios of the target concentration to background.
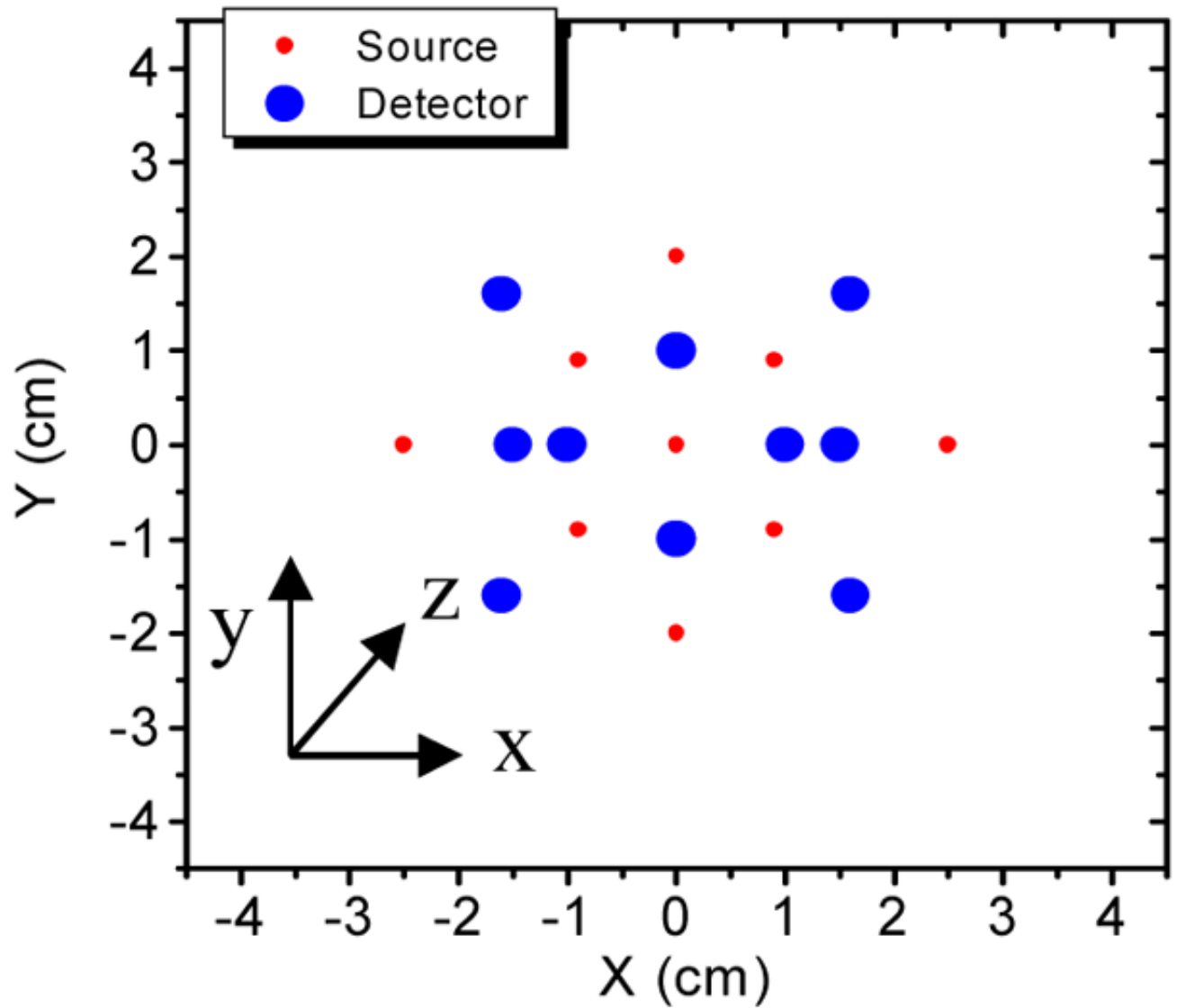
Fig. 2.
The schematic of the optical probe. The total imaging region underneath the probe is 9×9×4 (X, Y, Z) cm^3, which can be flexibly adjusted.
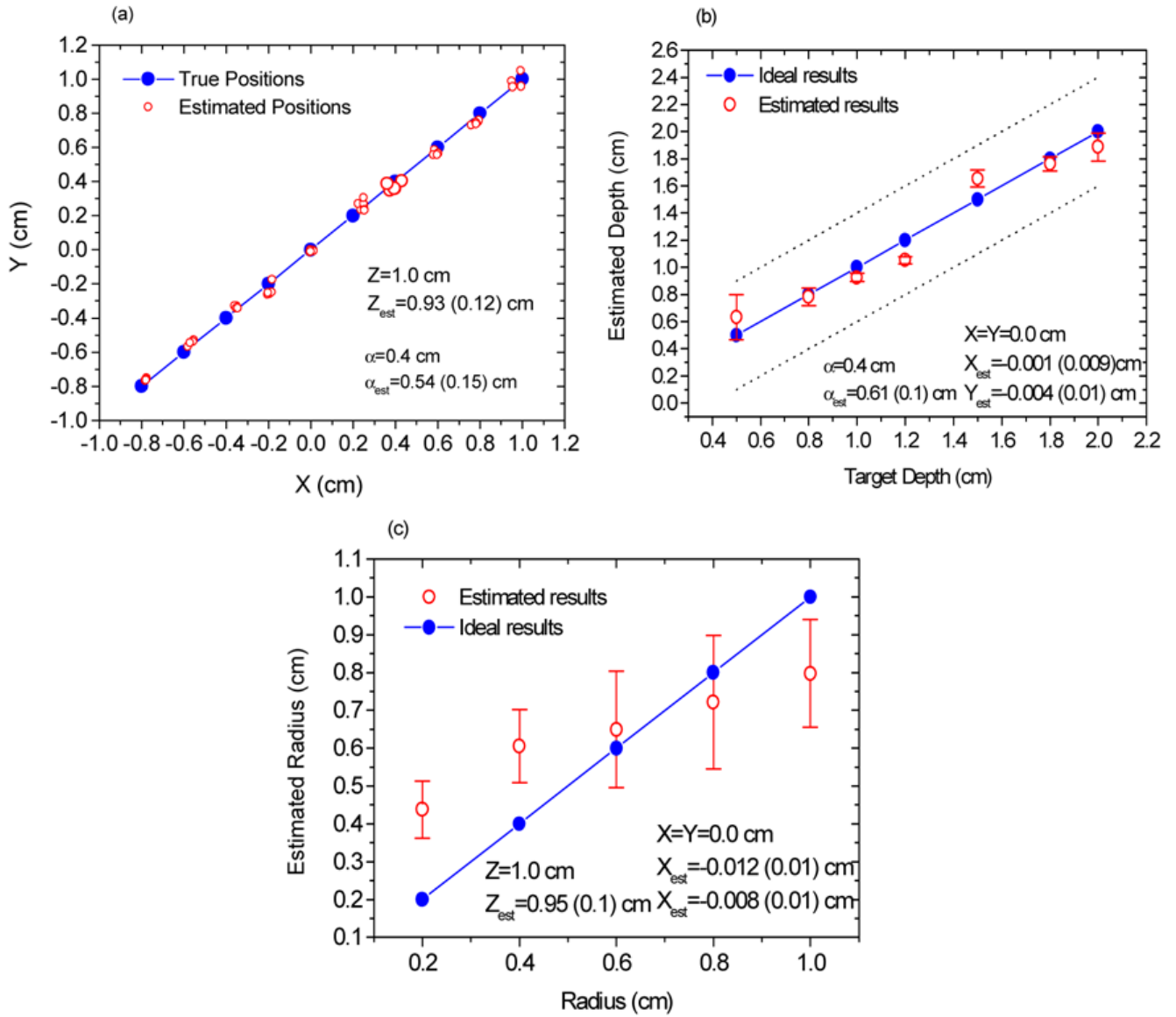
Fig. 3.
The structural parameters recovered from the simulation data. (a) Estimated X and Y, (b) Estimated depth Z, and (c) Estimated radius α versus their true values, respectively.
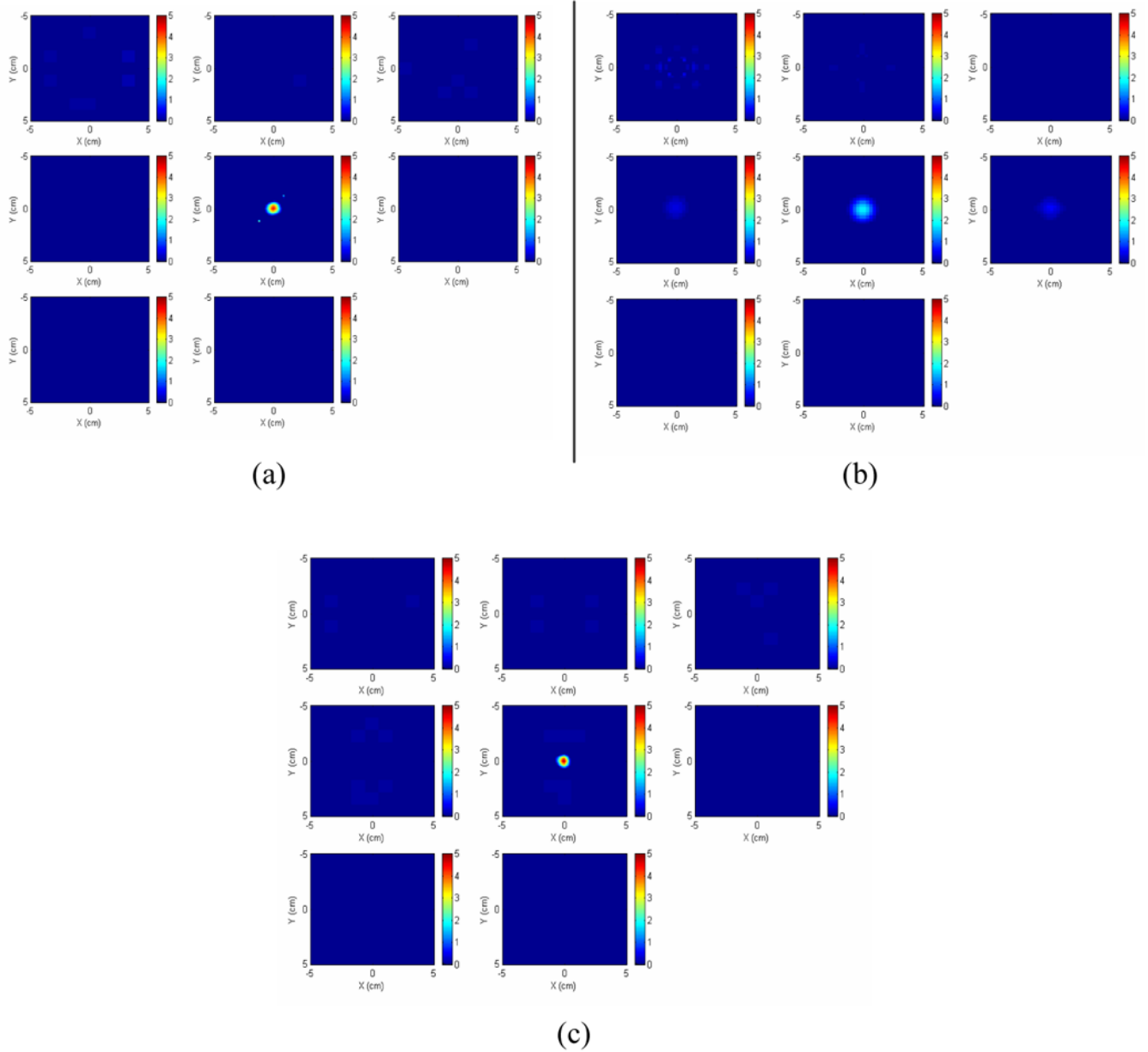
Fig. 4.
(a) Images reconstructed from the simulated data (added with noise) using dual-zone mesh. The center of the target is located at X=Y=0.0 cm, Z=2.5 cm. The radius of the spherical target is 0.4 cm. The slices at the first row from left to right correspond to imaging depth of 0.5 cm, 1.0 cm and 1.5 cm, respectively. The slices at the second row from left to right correspond to imaging depth of 2.0 cm, 2.5 cm, and 3.0 cm, respectively. The slices at the third row correspond to imaging depth of 3.5 cm and 4.0 cm, respectively. (b) The reconstructed images with single mesh obtained from the same data. (c) The reconstructed images based on the parameters used in (a) except background parameters (see the background parameters in *Sec. 4.1.2*).
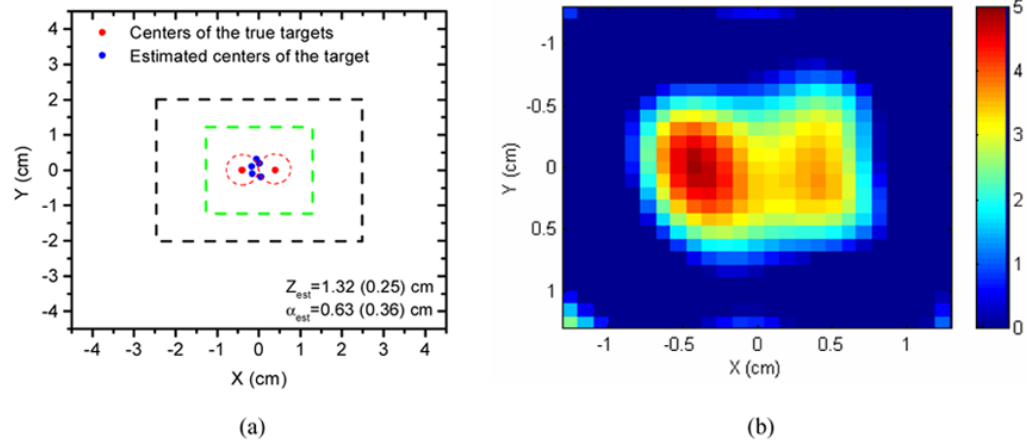
Fig. 5.
Reconstruction results of two targets: (a) Reconstructed structural parameters; the red dash circles in (a) represent the positions of the two targets and the blue dots are the estimated positions. The green dashed square indicates the target region and the black dashed square shows the region where the sources and the detectors are distributed. (b) Reconstructed fluorophore concentration distribution within the region marked by the green dashed square in (a). Note the image size is 3 cm by 3 cm, which is 1/3 of the image size used in Fig. 4 for each slice.
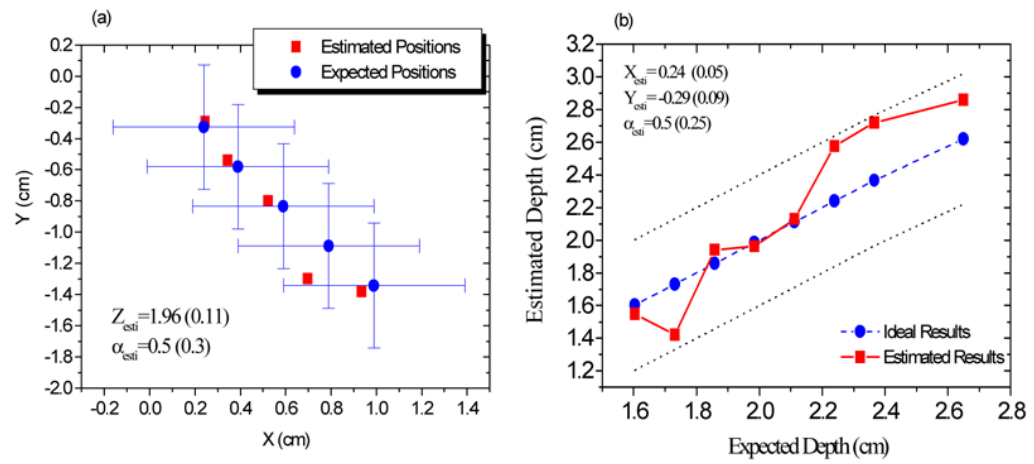
Fig. 6.
The structural parameters recovered from the experimental data. (a) the estimated X and Y, and (b) the estimated depth Z versus their expected values, respectively.
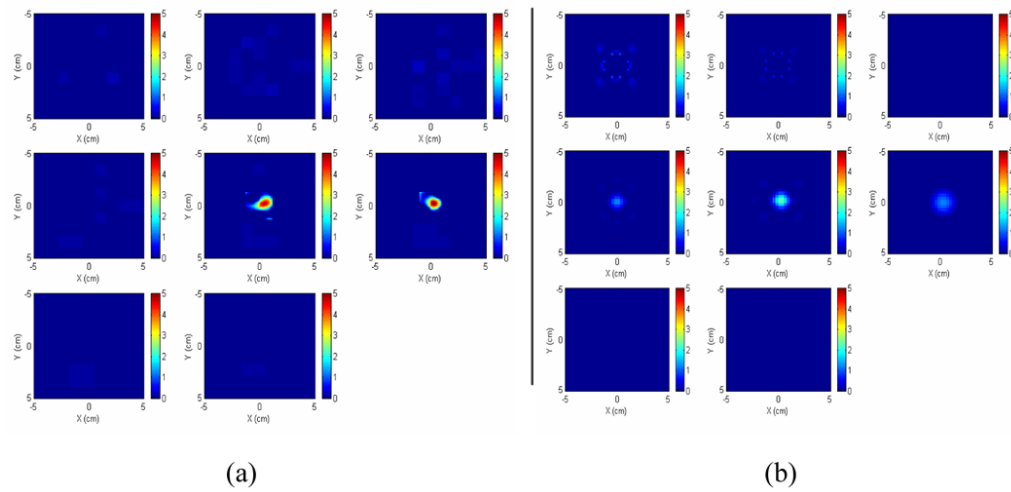
(a)

(b)

Fig. 7.
(a) Images reconstructed from the experimental data with dual-zone mesh. The center of the target is located at X= 0.24 cm, Y= −0.33 cm, and Z=2.65 cm. The target is a 0.4×0.4×0.4 cm^3 cube. The imaging depth used for each slice is the same as Fig. 4. The reconstructed images occur at both the fifth and sixth slices, which corresponds to imaging depths of 2.5 cm and 3.0 cm, respectively. (b) The reconstructed images with single mesh from the same data.

Table 1

Background parameters of the medium. $\mu_{a,660}^{c}$ and $\mu'_{s,660}$ were measured by the method used in Ref.[39]. $\mu_{a,694}^{c}$ and $\mu'_{s,694}$ were extracted by fitting the experimental data of the homogeneous Cy5.5 solution to the theoretical data based on the measured values of $\mu_{a,660}^{c}$ and $\mu'_{s,660}$. ε_{660} and ε_{694} were approximated from the maximum molar excitation coefficient of Cy5.5 in water ($0.25\ cm^{-1}\mu M^{-1}$) at 675 nm. Units of the absorption and scattering coefficients are cm^{-1}.

$\mu_{a,660}^{c}$	$\mu_{a,694}^{c}$	ε_{660}	ε_{694}	$\mu'_{s,660}$	$\mu'_{s,694}$
0.009	0.013	0.25/2	0.25/3	5.0	4.0